

Tenth-order lepton $g-2$: Contribution of some fourth-order radiative corrections to the sixth-order $g-2$ containing light-by-light-scattering subdiagrams

T. Aoyama,^{1,2} M. Hayakawa,^{1,2,3} T. Kinoshita,^{2,4} and M. Nio²

¹*Kobayashi-Maskawa Institute for the Origin of Particles and the Universe (KMI),*

Nagoya University, Nagoya, 464-8602, Japan

²*Theoretical Physics Laboratory, Nishina Center, RIKEN, Wako, 351-0198, Japan*

³*Department of Physics, Nagoya University, Nagoya, 464-8602, Japan*

⁴*Laboratory for Elementary Particle Physics,
Cornell University, Ithaca, New York, 14853, U.S.A*

Abstract

This paper reports the tenth-order QED contribution to lepton $g-2$ from diagrams of three gauge-invariant sets VI(d), VI(g), and VI(h), which are obtained by including various fourth-order radiative corrections to the sixth-order $g-2$ containing light-by-light-scattering subdiagrams. In the case of electron $g-2$, they consist of 492, 480, and 630 vertex Feynman diagrams, respectively. The results of numerical integration, including mass-dependent terms containing muon loops, are 1.8418 (95) $(\alpha/\pi)^5$ for the Set VI(d), -1.5918 (65) $(\alpha/\pi)^5$ for the Set VI(g), and 0.1797 (40) $(\alpha/\pi)^5$ for the Set VI(h), respectively. We also report the contributions to the muon $g-2$, which derive from diagrams containing an electron, muon or tau lepton loop: Their sums are -5.876 (802) $(\alpha/\pi)^5$ for the Set VI(d), 5.710 (490) $(\alpha/\pi)^5$ for the Set VI(g), and -8.361 (232) $(\alpha/\pi)^5$ for the Set VI(h), respectively.

PACS numbers: 13.40.Em, 14.60.Cd, 12.20.Ds, 06.20.Jr

I. INTRODUCTION

The anomalous magnetic moment $g-2$ of the electron is one of the most vigorously studied physical quantities at present, which provides a very stringent test of the validity of quantum electrodynamics (QED). To match the precision of the latest measurement of electron $g-2$ [1] the theory must include the QED radiative correction up to the eighth order [2–4] as well as the hadronic contribution [5–12] and the electroweak contribution [13–15] within the context of the standard model. As a matter of fact, the largest theoretical uncertainty now comes from the tenth-order QED contribution which has not yet been evaluated and is given only a crude estimate [16]. Thus it is an urgent matter to evaluate the actual value of the tenth-order term. To accomplish this task we started a systematic program several years ago to evaluate the complete tenth-order contribution [17–22].

The tenth-order QED contribution to the electron $g-2$ consists of the mass-independent term $A_1^{(10)}$ and the mass-dependent terms $A_2^{(10)}$ and $A_3^{(10)}$ in which muon and/or tau lepton loop is involved, which may be expressed as

$$a_e^{(10)} = \left[A_1^{(10)} + A_2^{(10)}(m_e/m_\mu) + A_2^{(10)}(m_e/m_\tau) + A_3^{(10)}(m_e/m_\mu, m_e/m_\tau) \right] \left(\frac{\alpha}{\pi} \right)^5. \quad (1)$$

The mass-independent term $A_1^{(10)}$ may be classified into six sets and further divided into 32 gauge-invariant subsets according to the type of the closed lepton loop subdiagram. Thus far, the numerical evaluation of 21 subsets has been carried out and the results were published [17–22].

In this paper we focus our attention on the gauge-invariant set VI which consists of all diagrams containing a light-by-light-scattering subdiagram, one of whose photon vertex is external. (We call this an *external* light-by-light-scattering subdiagram.) Of eleven gauge-invariant subsets of the Set VI, eight have been evaluated previously [17]. The purpose of this paper is to report the evaluation of the remaining three gauge-invariant subsets: Sets VI(d), VI(g), and VI(h). In diagrams of Set VI(d) two virtual photon lines are attached to the open lepton line. This set contains 492 vertex diagrams. In diagrams of Set VI(g) one virtual photon line is attached to the open lepton line and the other virtual photon line is attached to the closed lepton loop. This set contains 480 vertex diagrams. In diagrams of Set VI(h) two virtual photon lines are attached to the closed lepton loop. This set contains 630 vertex diagrams. Typical diagrams of these sets are shown in Fig. 1.

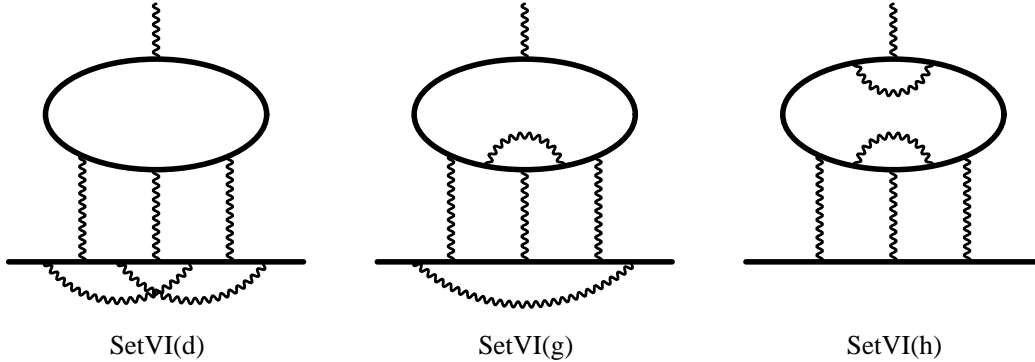


FIG. 1: Typical diagrams of Set VI(d), Set VI(g), and Set VI(h).

Our numerical evaluation of Feynman diagrams is based on the parametric integration formula [23–25]. To handle a relatively large number of diagrams systematically without errors, we developed an automated code-generating system called GENCODELLN that produces FORTRAN codes for the numerical integration. It is an adaptation of the previously developed system for the type of diagrams without lepton loops [18, 19] to the diagrams containing an external light-by-light-scattering subdiagram.

This paper is organized as follows. Section II describes our scheme for numerical evaluation. Section III gives the results of the numerical evaluation. Section IV is devoted to the summary and discussion. In Appendix we describes an algorithm for identifying independent set of loops on a diagram that is required for constructing the amplitude. For simplicity the factor $(\alpha/\pi)^5$ is omitted in Secs. II and III.

II. NUMERICAL EVALUATION SCHEME

In this section we describe our scheme for the numerical evaluation of the diagrams of Sets VI(d), VI(g), and VI(h). The diagram that belongs to these sets consists of an open lepton line (ℓ_1) and a closed lepton loop (ℓ_2) that forms a light-by-light-scattering (*l-by-l*) subdiagram, where ℓ_1 and ℓ_2 refer to the types of leptons, i.e. electron (e), muon (m), or tau lepton (t). The mass-dependence of these diagrams and amplitudes is characterized by (ℓ_1, ℓ_2) or by superscript $^{(\ell_1 \ell_2)}$.

We adopt a relation derived from the Ward-Takahashi identity

$$\Lambda^\nu(p, q) \simeq -q^\mu \left. \frac{\partial \Lambda_\mu(p, q)}{\partial q_\nu} \right|_{q \rightarrow 0} - \frac{\partial \Sigma(p)}{\partial p_\nu} \quad (2)$$

where $\Lambda^\nu(p, q)$ is the sum of proper vertex parts which are obtained by inserting an external photon vertex in the lepton lines of the self-energy function $\Sigma(p)$ of a diagram \mathcal{G} in all possible ways. Taking account of the charge conjugation and time reversal symmetry the numbers of independent integrals to evaluate become 45 for Set VI(d) (see Fig. 2), 26 for Set VI(g) (see Fig. 3), and 27 for Set VI(h) (see Fig. 4).

The amplitude of a Feynman diagram is turned into an integral over the Feynman parameters assigned to the lepton and photon lines by using the parametric integral formula [23]. Note that the contribution of the second term on the right-hand side of Eq. (2) vanishes due to the Furry's theorem.

In our numerical procedure the renormalization of the amplitude is carried out by the subtractive renormalization. The unrenormalized amplitude $M_{\mathcal{G}}$ of a diagram \mathcal{G} is related to a finite calculable quantity $\Delta M_{\mathcal{G}}$ by appropriate subtraction terms of UV and IR divergences. These subtraction terms are prepared in the form of integrals over the same Feynman parameter space so that they cancel out the divergent behavior of the original unrenormalized integral *point-by-point*.

The UV divergence arising from the l-by-l subdiagram must be regularized, e.g., by the Pauli-Villars regularization. However, in Eq. (2) the Ward-Takahashi-summed amplitude is given as the differentiation of $\Lambda^\mu(p, q)$ with respect to q_ν . Therefore the divergence from the l-by-l loop is lifted, and the PV regularization is no longer needed.

As a consequence the source of the UV divergences resides only in the vertex and self-energy subdiagrams of second and fourth order. These divergences are handled by K operation [24, 26]. By definition the K operation yields the subtraction integral which is analytically factorizable into a product or a sum of products of lower-order quantities. It is symbolically denoted by

$$\mathbb{K}_S M_{\mathcal{G}} = L_S^{\text{UV}} M_{\mathcal{G}/S}, \quad (3)$$

when S is a vertex subdiagram, and by

$$\mathbb{K}_S M_{\mathcal{G}} = \delta m_S^{\text{UV}} M_{\mathcal{G}/S} + B_S^{\text{UV}} M_{[\mathcal{G}/S, i]}, \quad (4)$$

when S is a self-energy subdiagram. Here, the superscript UV means that the leading UV

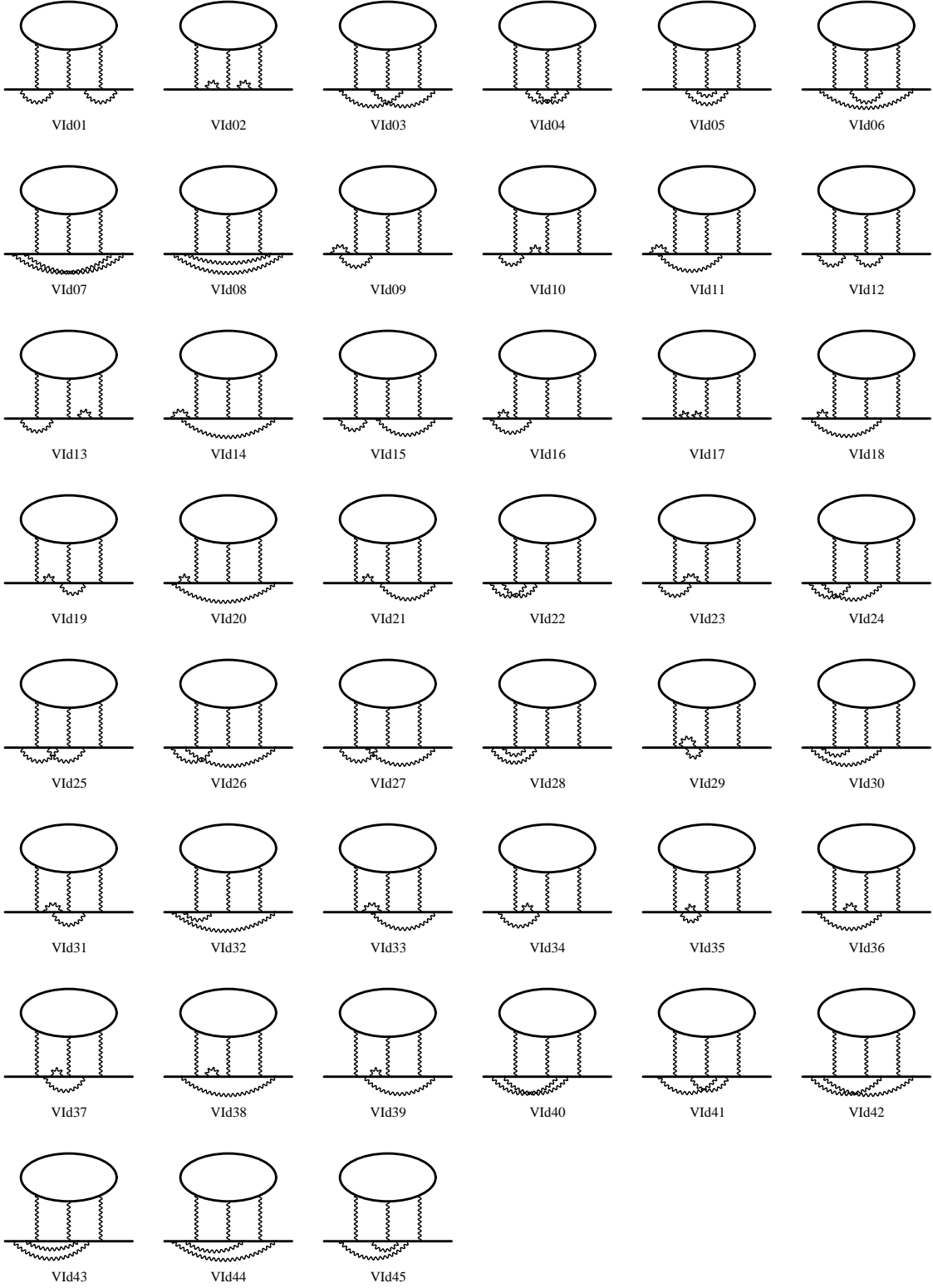


FIG. 2: The contribution of Set VI(d) is represented by 45 independent diagrams as listed.

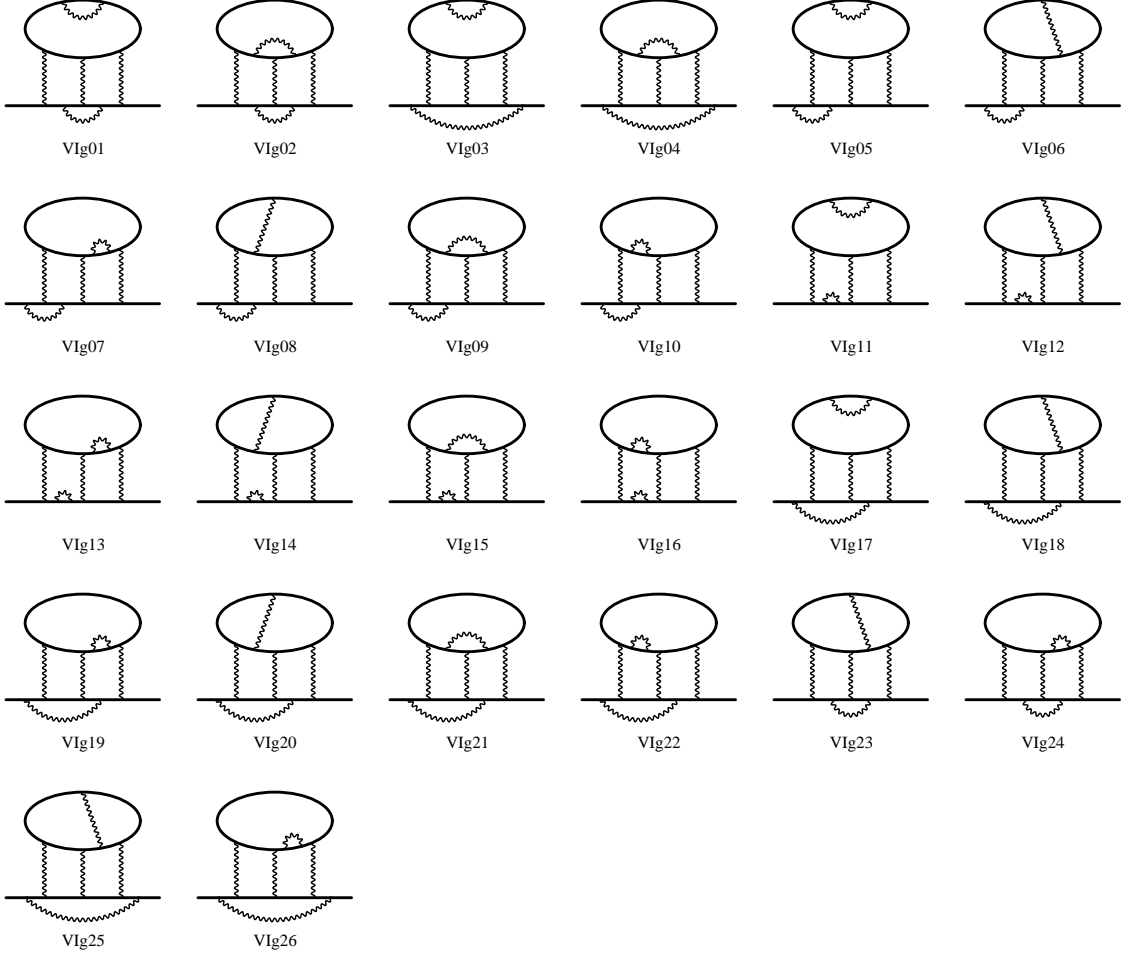


FIG. 3: The contribution of Set VI(g) is represented by 26 independent diagrams as listed.

divergent part is taken for the vertex renormalization constant L , the mass renormalization constant δm , and the wave-function renormalization constant B , respectively. Note that $\delta m_2^{\text{UV}} = \delta m_2$. We also apply R subtraction [19] by which the residual part $\widetilde{\delta m} \equiv \delta m - \delta m^{\text{UV}}$ of the fourth-order mass renormalization constant is subtracted away to accomplish complete subtraction of δm .

Some diagrams of Set VI(d) and Set VI(g) have IR divergences. For example, the diagram VIg04 of Set VI(g) shown in Fig. 3, in which a photon line attached to the open lepton line at both ends encloses an eighth-order l-by-l subdiagram, exhibits an IR divergence when this outermost photon goes soft. These divergences are subtracted away by I subtraction [19]. By construction the I subtraction term factorizes as

$$\mathbb{I}_S M_G = M_S \widetilde{L}_{G/S,i}, \quad (5)$$

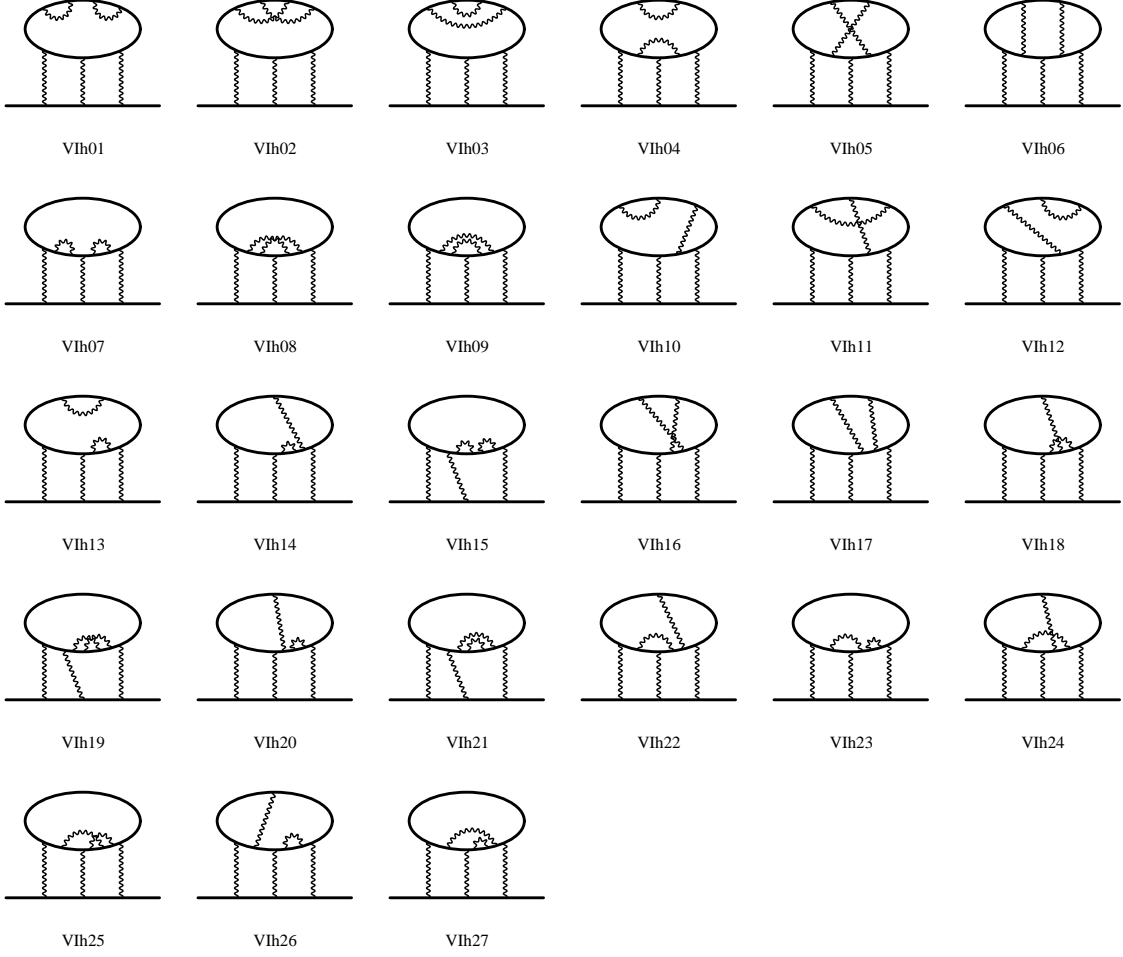


FIG. 4: The contribution of Set VI(h) is represented by 27 independent diagrams as listed.

where $\tilde{L} \equiv L - L^{\text{UV}}$ denotes the residual part of the vertex renormalization constant.

The finite amplitude $\Delta M_{\mathcal{G}}$ obtained so far differs from the standard renormalized quantity, because the subtraction terms involve only a fraction of the renormalization constants relevant to the divergences. To achieve the standard on-the-mass-shell renormalization, the differences are collected over the diagrams of the subset, which is finite, and added to $\Delta M_{\mathcal{G}}$. This step is called the residual renormalization.

The exactly renormalized contributions of Sets VI(d), VI(g), and VI(h) to the magnetic

moment are given by the formulas:

$$\begin{aligned} a_{\ell_1}^{(10)}[\text{VI(d)}^{(\ell_1\ell_2)}] &= \Delta M_{\text{VI(d)}}^{(\ell_1\ell_2)} - 4\Delta LB_2 \Delta M_{\text{IVc}}^{(\ell_1\ell_2)} + (-2\Delta LB_4 + 5(\Delta LB_2)^2) a_{6\text{LL}}^{(\ell_1\ell_2)} \\ &= \Delta M_{\text{VI(d)}}^{(\ell_1\ell_2)} - 4\Delta LB_2 a_{\text{IVc}}^{(\ell_1\ell_2)} - (2\Delta LB_4 + 3(\Delta LB_2)^2) a_{6\text{LL}}^{(\ell_1\ell_2)}, \end{aligned} \quad (6)$$

$$\begin{aligned} a_{\ell_1}^{(10)}[\text{VI(g)}^{(\ell_1\ell_2)}] &= \Delta M_{\text{VI(g)}}^{(\ell_1\ell_2)} - 2\Delta LB_2 \Delta M_{\text{IVb}}^{(\ell_1\ell_2)} - 3\Delta LB_2 \Delta M_{\text{IVc}}^{(\ell_1\ell_2)} + 6(\Delta LB_2)^2 a_{6\text{LL}}^{(\ell_1\ell_2)} \\ &= \Delta M_{\text{VI(g)}}^{(\ell_1\ell_2)} - 2\Delta LB_2 a_{\text{IVb}}^{(\ell_1\ell_2)} - 3\Delta LB_2 a_{\text{IVc}}^{(\ell_1\ell_2)} - 6(\Delta LB_2)^2 a_{6\text{LL}}^{(\ell_1\ell_2)}, \end{aligned} \quad (7)$$

$$\begin{aligned} a_{\ell_1}^{(10)}[\text{VI(h)}^{(\ell_1\ell_2)}] &= \Delta M_{\text{VI(h)}}^{(\ell_1\ell_2)} - 5\Delta LB_2 \Delta M_{\text{IVb}}^{(\ell_1\ell_2)} + (-3\Delta LB_4 + 9(\Delta LB_2)^2) a_{6\text{LL}}^{(\ell_1\ell_2)} \\ &= \Delta M_{\text{VI(h)}}^{(\ell_1\ell_2)} - 5\Delta LB_2 a_{\text{IVb}}^{(\ell_1\ell_2)} - (3\Delta LB_4 + 6(\Delta LB_2)^2) a_{6\text{LL}}^{(\ell_1\ell_2)}. \end{aligned} \quad (8)$$

Here, $\Delta M_{\text{VI(d)}}$, $\Delta M_{\text{VI(g)}}$, and $\Delta M_{\text{VI(h)}}$ are the sum of the finite amplitude of the diagrams within the subsets VI(d), VI(g), and VI(h), respectively. $a_{6\text{LL}}$ is the sixth-order anomalous magnetic moment containing the fourth-order l-by-l diagram. a_{IVb} and a_{IVc} are the eighth-order anomalous magnetic moments of the set of diagrams containing the external l-by-l subdiagram with a virtual photon line attached to the lepton loop (IVb) or to the open lepton line (IVc). ΔM_{IVb} and ΔM_{IVc} are their finite part defined in Ref. [26]. ΔLB_2 and ΔLB_4 are the sum of the finite part of vertex and wave-function renormalization constants of second and fourth order, respectively.

The code-generating program GENCODELLN takes a one-line representation of a diagram as an input, and generates the numerical integration program formatted in FORTRAN. During this process it finds the form of the unrenormalized amplitudes, identifies the divergence structure, and constructs the UV- and/or IR-subtraction integrals. The symbolic manipulations concerning e.g the gamma matrix calculus and the analytic integration using homemade integration tables are processed with the helps of FORM [27] and Maple.

III. RESULTS

The numerical integration is carried out using the adaptive-iterative Monte-Carlo integration routine VEGAS [28]. The numerical values of individual amplitudes of Set VI(d), Set VI(g), and Set VI(h) are listed in Tables I, II, and III, respectively, for the mass-independent term and the mass-dependent terms in which $(\ell_1, \ell_2) = (e, m)$, (m, e) , and (m, t) . We use the muon-electron mass ratio $m_\mu/m_e = 206.768\,282\,3$ (52) and the tau-muon mass ratio $m_\tau/m_\mu = 16.818\,3$ (27) for numerical evaluation [16].

A. Mass-independent contribution

Let us first consider the case in which ℓ_1 and ℓ_2 are of the same type of lepton, i.e., $\ell_1 = \ell_2 = e, m$, or t . This gives a mass-independent contribution to the lepton $g-2$. The numerical values are listed in the second columns of Table I for Set VI(d), Table II for Set VI(g), and Table III for Set VI(h), respectively. The values of the sixth- and eighth-order amplitudes and the finite renormalization constants are listed in Table IV. Putting these values into Eqs. (6), (7), and (8), the mass-independent contributions A_1 of the respective subsets are:

$$A_1^{(10)}[\text{Set VI(d)}] = 1.840\ 5\ (95), \quad (9)$$

$$A_1^{(10)}[\text{Set VI(g)}] = -1.591\ 3\ (65), \quad (10)$$

$$A_1^{(10)}[\text{Set VI(h)}] = 0.179\ 7\ (40). \quad (11)$$

B. Mass-dependent contribution (e, m)

The mass-dependent contribution to the electron $g-2$ in which the light-by-light-scattering subdiagram consists of the muon loop, i.e., $\ell_1 = e$ and $\ell_2 = m$, is found from the numerical values listed in the third columns of Table I for Set VI(d), Table II for Set VI(g), and Table III for Set VI(h), respectively. The values of the mass-dependent sixth- and eighth-order amplitudes are listed in Table IV. Putting these values into Eqs. (6), (7), and (8), we obtain the mass-dependent contributions $A_2(m_e/m_\mu)$ of the respective subsets:

$$A_2^{(10)}(m_e/m_\mu)[\text{Set VI(d)}] = 0.001\ 276\ (76), \quad (12)$$

$$A_2^{(10)}(m_e/m_\mu)[\text{Set VI(g)}] = -0.000\ 497\ (29), \quad (13)$$

$$A_2^{(10)}(m_e/m_\mu)[\text{Set VI(h)}] = 0.000\ 045\ (10). \quad (14)$$

C. Mass-dependent contribution (m, e)

Similarly, the mass-dependent contribution to the muon $g-2$ in which the light-by-light-scattering subdiagram consists of the electron loop, i.e., $\ell_1 = m$ and $\ell_2 = e$, is found from the numerical values listed in the fourth column of Tables I, II, and III. Their contributions

are:

$$A_2^{(10)}(m_\mu/m_e)[\text{Set VI(d)}] = -7.798 \text{ (801)}, \quad (15)$$

$$A_2^{(10)}(m_\mu/m_e)[\text{Set VI(g)}] = 7.346 \text{ (489)}, \quad (16)$$

$$A_2^{(10)}(m_\mu/m_e)[\text{Set VI(h)}] = -8.546 \text{ (231)}. \quad (17)$$

D. Mass-dependent contribution (m, t)

The mass-dependent contribution of the tau-lepton loop to the muon $g-2$ is also evaluated and their numerical values are listed in the fifth column of Tables I, II, and III. The results are

$$A_2^{(10)}(m_\mu/m_\tau)[\text{Set VI(d)}] = 0.081 \text{ 77 (161)}, \quad (18)$$

$$A_2^{(10)}(m_\mu/m_\tau)[\text{Set VI(g)}] = -0.044 \text{ 51 (96)}, \quad (19)$$

$$A_2^{(10)}(m_\mu/m_\tau)[\text{Set VI(h)}] = 0.004 \text{ 85 (46)}. \quad (20)$$

IV. SUMMARY AND DISCUSSIONS

In this paper we evaluated the tenth-order QED corrections to the anomalous magnetic moments of electron and muon from the sets of diagrams, VI(d), VI(g), and VI(h).

For the electron $g-2$, the total contribution is the sum of the mass-independent terms (9), (10), and (11) and the mass-dependent terms involving the muon loops (12), (13), and (14):

$$a_e[\text{Set VI(d)}] = 1.841 \text{ 8 (95)} \left(\frac{\alpha}{\pi}\right)^5, \quad (21)$$

$$a_e[\text{Set VI(g)}] = -1.591 \text{ 8 (65)} \left(\frac{\alpha}{\pi}\right)^5, \quad (22)$$

$$a_e[\text{Set VI(h)}] = 0.179 \text{ 7 (40)} \left(\frac{\alpha}{\pi}\right)^5. \quad (23)$$

The tau-lepton contributions to a_e are more than an order of magnitude smaller than Eqs. (12), (13), and (14) and lie within the uncertainties of Eqs. (21), (22), and (23). Thus they are negligible at present.

For the muon $g-2$, the contributions are the sums of the mass-independent terms (9), (10), and (11) and the mass-dependent terms involving electron loops (15), (16), and (17)

TABLE I: Numerical values of diagrams of Set VI(d) for the mass-independent contributions (e, e) and the mass-dependent contributions (e, m), (m, e), and (m, t). The numerals in the parentheses show the uncertainty of the numerical integration carried out using VEGAS. The number of sampling points is 10^9 times approximately 100 iterations.

Diagram	$\Delta M^{(ee)}$	$\Delta M^{(em)}$	$\Delta M^{(me)}$	$\Delta M^{(mt)}$
VId01	0.38496 (108)	0.0002512 (167)	81.810 (140)	0.01307 (27)
VId02	0.38884 (73)	0.0000244 (29)	170.126 (91)	0.00169 (9)
VId03	-0.09728 (10)	-0.0000264 (4)	4.054 (3)	-0.00212 (1)
VId04	0.31560 (20)	0.0000499 (20)	10.720 (14)	0.00448 (5)
VId05	-0.02779 (18)	0.0000489 (39)	16.903 (20)	0.00158 (6)
VId06	-0.19938 (42)	-0.0001046 (46)	-78.953 (47)	-0.00548 (10)
VId07	-0.13469 (149)	-0.0000488 (66)	-53.367 (97)	-0.00240 (21)
VId08	0.16511 (99)	0.0000495 (14)	140.628 (93)	0.00268 (8)
VId09	0.66926 (342)	0.0002166 (212)	160.196 (211)	0.01340 (54)
VId10	-0.86487 (129)	-0.0003050 (90)	-240.503 (138)	-0.01865 (24)
VId11	0.19659 (187)	0.0000178 (131)	82.026 (122)	0.00213 (33)
VId12	0.68550 (148)	0.0003757 (439)	104.960 (170)	0.02205 (61)
VId13	-0.84151 (119)	-0.0002828 (88)	-236.280 (142)	-0.01644 (22)
VId14	-0.55165 (292)	-0.0000066 (105)	-241.783 (166)	-0.00146 (37)
VId15	0.40793 (247)	0.0002465 (180)	74.465 (151)	0.01367 (43)
VId16	-0.86278 (165)	-0.0002389 (100)	-194.970 (108)	-0.01590 (31)
VId17	0.72320 (103)	0.0000980 (53)	335.970 (402)	0.00704 (14)
VId18	-0.12727 (164)	0.0002904 (71)	-105.046 (87)	0.01107 (22)
VId19	-0.68392 (101)	-0.0002279 (214)	-142.105 (98)	-0.01381 (36)
VId20	0.51681 (295)	0.0001113 (72)	293.527 (151)	0.00712 (33)
VId21	-0.84441 (81)	-0.0003483 (23)	-103.944 (70)	-0.02040 (8)
VId22	0.32927 (138)	0.0000666 (71)	37.656 (85)	0.00574 (20)
VId23	0.30074 (175)	0.0002004 (126)	90.028 (135)	0.01021 (31)
VId24	-0.06021 (14)	0.0000016 (4)	11.053 (10)	-0.00019 (2)
VId25	0.20753 (13)	0.0000311 (3)	18.408 (11)	0.00277 (1)
VId26	0.55652 (97)	0.0001401 (44)	30.649 (32)	0.01020 (12)
VId27	0.04473 (69)	-0.0000219 (31)	17.953 (21)	-0.00182 (9)
VId28	0.19223 (194)	0.0001718 (146)	78.298 (170)	0.00875 (33)
VId29	-0.55884 (161)	-0.0001263 (71)	-306.257 (141)	-0.00673 (21)
VId30	0.23422 (35)	0.0002785 (65)	29.833 (34)	0.01403 (11)
VId31	0.13852 (41)	0.0001240 (86)	50.343 (58)	0.00596 (12)
VId32	-0.65225 (160)	-0.0002349 (53)	-287.636 (156)	-0.01276 (20)
VId33	0.30989 (145)	0.0002517 (96)	38.190 (111)	0.01293 (21)
VId34	-0.74797 (115)	-0.0002863 (61)	-158.487 (118)	-0.01729 (17)
VId35	0.36986 (130)	0.0002577 (77)	229.607 (120)	0.01267 (23)
VId36	-0.69348 (77)	-0.0002695 (67)	-81.830 (36)	-0.01390 (14)
VId37	-0.40728 (48)	-0.0001806 (87)	-80.159 (48)	-0.01090 (17)
VId38	0.59921 (159)	0.0001969 (44)	357.390 (157)	0.01081 (16)
VId39	-0.46380 (126)	-0.0002631 (77)	-78.155 (82)	-0.01385 (21)
VId40	0.11874 (62)	0.0000125 (33)	12.521 (25)	0.00079 (9)
VId41	-0.07805 (16)	-0.0000071 (4)	9.202 (11)	-0.00079 (2)
VId42	0.11040 (83)	-0.0001267 (49)	21.555 (22)	-0.00420 (12)
VId43	-0.24138 (78)	-0.0000597 (39)	18.378 (39)	-0.00597 (11)
VId44	-0.12923 (169)	0.0000835 (48)	-123.103 (97)	0.00486 (20)
VId45	0.37295 (35)	0.0003013 (64)	23.573 (31)	0.01616 (11)
total	-0.92943 (941)	0.0007324 (757)	37.443 (801)	0.03080 (158)

TABLE II: Numerical values of diagrams of Set VI(g) for the mass-independent contributions (e, e) and the mass-dependent contributions (e, m), (m, e), and (m, t). The numerals in the parentheses show the uncertainty of the numerical integration carried out using VEGAS. The number of sampling points is 10^9 times approximately 100 iterations.

Diagram	$\Delta M^{(ee)}$	$\Delta M^{(em)}$	$\Delta M^{(me)}$	$\Delta M^{(mt)}$
VIg01	-0.63173 (62)	0.0008231 (30)	-52.384 (64)	0.01498 (11)
VIg02	0.31956 (36)	-0.0001824 (14)	34.460 (47)	-0.00257 (5)
VIg03	0.98647 (72)	0.0009548 (12)	130.839 (34)	0.04157 (6)
VIg04	-0.29176 (64)	-0.0002605 (8)	-81.920 (72)	-0.01137 (5)
VIg05	-2.19013 (217)	0.0001161 (105)	-185.978 (166)	-0.02197 (39)
VIg06	0.72494 (122)	0.0005969 (46)	116.641 (99)	0.02417 (17)
VIg07	-2.30397 (241)	-0.0013244 (98)	-178.720 (160)	-0.06282 (37)
VIg08	1.00663 (111)	0.0004722 (48)	109.909 (85)	0.01977 (16)
VIg09	0.77315 (138)	0.0000200 (54)	117.911 (124)	0.00743 (19)
VIg10	-1.00933 (221)	-0.0004571 (123)	-182.581 (183)	-0.01757 (43)
VIg11	1.84018 (81)	0.0013280 (19)	275.717 (58)	0.04634 (9)
VIg12	-1.22515 (69)	-0.0003466 (12)	-179.818 (84)	-0.02208 (6)
VIg13	2.96666 (99)	0.0003162 (20)	271.391 (71)	0.03606 (10)
VIg14	-1.30518 (79)	0.0001885 (14)	-172.175 (72)	-0.00348 (6)
VIg15	-0.60441 (83)	-0.0003888 (13)	-182.323 (83)	-0.01435 (6)
VIg16	1.99802 (100)	-0.0007980 (22)	275.112 (62)	-0.01361 (10)
VIg17	-1.85498 (142)	-0.0017517 (48)	-87.674 (94)	-0.07228 (20)
VIg18	0.81225 (82)	-0.0000606 (21)	58.248 (58)	0.00235 (8)
VIg19	0.06430 (143)	0.0015046 (46)	-88.590 (94)	0.05249 (20)
VIg20	0.11993 (77)	-0.0003910 (17)	65.647 (60)	-0.01272 (8)
VIg21	0.55442 (100)	0.0004771 (22)	58.433 (83)	0.01918 (10)
VIg22	-1.87621 (202)	-0.0002371 (60)	-88.324 (126)	-0.02794 (25)
VIg23	0.72649 (53)	0.0009910 (23)	57.310 (59)	0.03702 (9)
VIg24	-1.42022 (129)	-0.0018534 (60)	-101.191 (102)	-0.06842 (19)
VIg25	-0.60245 (102)	0.0002251 (16)	-164.454 (84)	0.00559 (9)
VIg26	0.75452 (110)	-0.0007759 (27)	258.476 (81)	-0.02489 (13)
total	1.66799 (642)	0.0008141 (286)	3.961 (489)	0.06914 (93)

and tau-lepton loop (18), (19), and (20):

$$a_\mu[\text{Set VI(d)}] = -5.876 (802) \left(\frac{\alpha}{\pi}\right)^5, \quad (24)$$

$$a_\mu[\text{Set VI(g)}] = 5.710 (490) \left(\frac{\alpha}{\pi}\right)^5, \quad (25)$$

$$a_\mu[\text{Set VI(h)}] = -8.361 (232) \left(\frac{\alpha}{\pi}\right)^5. \quad (26)$$

Acknowledgments

This work is supported in part by JSPS Grant-in-Aid for Scientific Research (C)19540322 and (C)20540261. T. K.'s work is supported in part by the U. S. National Science Foundation under Grant PHY-0757868, and the International Exchange Support Grants (FY2010) of

TABLE III: Numerical values of diagrams of Set VI(h) for the mass-independent contributions (e, e) and the mass-dependent contributions (e, m) , (m, e) , and (m, t) . The numerals in the parentheses show the uncertainty of the numerical integration carried out using VEGAS. The number of sampling points is 10^9 times approximately 100 iterations.

Diagram	$\Delta M^{(ee)}$	$\Delta M^{(em)}$	$\Delta M^{(me)}$	$\Delta M^{(mt)}$
VIh01	0.35996 (46)	-0.0009939 (6)	126.906 (17)	-0.04544 (4)
VIh02	0.27086 (37)	0.0006152 (4)	-73.046 (10)	0.03092 (3)
VIh03	-0.59951 (47)	-0.0007719 (4)	50.488 (9)	-0.03977 (3)
VIh04	0.26801 (45)	0.0001968 (4)	-95.157 (28)	0.01264 (3)
VIh05	0.13007 (35)	0.0000478 (6)	1.319 (2)	0.00311 (3)
VIh06	0.42117 (65)	0.0000669 (10)	69.018 (48)	0.00532 (5)
VIh07	3.15574 (62)	0.0010860 (7)	141.662 (20)	0.06653 (5)
VIh08	0.40673 (50)	0.0000576 (10)	41.392 (15)	0.00419 (5)
VIh09	0.02536 (48)	0.0000732 (8)	17.187 (22)	0.00327 (4)
VIh10	-2.49371 (74)	-0.0010322 (10)	-198.433 (40)	-0.05948 (6)
VIh11	-0.08174 (71)	0.0001225 (15)	42.256 (32)	0.00482 (8)
VIh12	-1.61239 (108)	-0.0011801 (32)	-94.032 (71)	-0.06307 (16)
VIh13	3.12210 (86)	0.0000566 (13)	262.754 (32)	0.01744 (10)
VIh14	-3.55461 (134)	-0.0011428 (30)	-209.006 (113)	-0.07210 (14)
VIh15	5.66905 (81)	0.0021336 (13)	273.980 (33)	0.12779 (10)
VIh16	0.64030 (76)	-0.0002009 (22)	78.458 (33)	-0.00650 (11)
VIh17	0.46696 (72)	0.0001387 (20)	35.527 (46)	0.00877 (10)
VIh18	0.41308 (68)	0.0001996 (15)	46.562 (34)	0.01193 (8)
VIh19	-2.53838 (76)	-0.0008088 (15)	-168.962 (29)	-0.05015 (9)
VIh20	1.06872 (116)	0.0008938 (31)	-86.585 (72)	0.04727 (16)
VIh21	2.24221 (70)	0.0009253 (14)	117.262 (29)	0.05466 (8)
VIh22	0.06791 (81)	-0.0001971 (15)	143.881 (80)	-0.00920 (9)
VIh23	-1.86591 (44)	-0.0001763 (4)	-212.603 (17)	-0.01768 (3)
VIh24	-0.03105 (50)	0.0000472 (12)	-3.201 (4)	0.00194 (6)
VIh25	-0.30141 (80)	-0.0001359 (21)	51.665 (47)	-0.00818 (12)
VIh26	-2.02809 (77)	-0.0004662 (12)	-198.376 (59)	-0.03184 (8)
VIh27	0.92582 (72)	0.0006938 (12)	-98.570 (41)	0.03794 (8)
total	4.54722 (393)	0.0002482 (90)	62.345 (231)	0.03516 (44)

RIKEN. T. K. thanks RIKEN for the hospitality extended to him while a part of this work is carried out. The numerical calculation was conducted on the RIKEN Super Combined Cluster (RSCC) and the RIKEN Integrated Cluster of Clusters (RICC) supercomputing systems.

Appendix: Algorithm for identifying independent loops

This Appendix describes an algorithm for identifying the fundamental set of circuits of a diagram following Ref. [33] which is adapted to automated handling by computers.

In the parametric integral approach, the integrand of the amplitude is expressed in terms of “building blocks”, B_{ij} , U , V , A_j , which are functions of Feynman parameters. B_{ij} reflects

TABLE IV: Auxiliary integrals for Sets VI(d), VI(g), and VI(h). The $g-2$ contribution from the sixth-order vertex diagram containing a light-by-light scattering subdiagram $a_6^{(\ell_1\ell_2)}$ is analytically known for arbitrary combinations of leptons (ℓ_1, ℓ_2) [29, 30]. The numerical values of mass-dependent terms (e, m) , (m, e) , and (m, t) are given in [31]. The eighth-order $g-2$ contributions from Group IV(b) and Group IV(c) diagrams with the lepton combinations (e, e) and (m, e) ($a_{\text{IVb}}^{(ee)}$, $a_{\text{IVb}}^{(me)}$, $a_{\text{IVc}}^{(ee)}$, and $a_{\text{IVc}}^{(me)}$) are quoted from [2, 32]. Other mass-dependent terms of these diagrams, $a_{\text{IVb}}^{(em)}$, $a_{\text{IVb}}^{(mt)}$, $a_{\text{IVc}}^{(em)}$, and $a_{\text{IVc}}^{(mt)}$, are newly evaluated in this paper. The forth- and second-order renormalization constants ΔLB_4 and ΔLB_2 are related to our previous notation through $\Delta LB_4 = \Delta L_4 + \Delta B_4$ and $\Delta LB_2 = \Delta B_2$ [2].

Integral	Value (error)	Integral	Value (error)
$a_6^{(ee)}$	0.371005292...	$a_6^{(em)}$	$1.439445989 (77) \times 10^{-5}$
$a_6^{(me)}$	20.94792489(16)	$a_6^{(mt)}$	0.00214283 (69)
$a_{\text{IVb}}^{(ee)}$	0.82249 (28)	$a_{\text{IVb}}^{(em)}$	0.00004105 (93)
$a_{\text{IVb}}^{(me)}$	-0.41704 (375)	$a_{\text{IVb}}^{(mt)}$	0.006106 (31)
$a_{\text{IVc}}^{(ee)}$	-1.13891 (35)	$a_{\text{IVc}}^{(em)}$	-0.0001897 (63)
$a_{\text{IVc}}^{(me)}$	2.90722 (444)	$a_{\text{IVc}}^{(mt)}$	-0.018233 (106)
ΔLB_4	0.027930 (28)	ΔLB_2	0.75

loop structure of the diagram, while A_j is related to the flow of the external momenta.

The definition of B_{ij} is given as follows [25]. A chain diagram $\tilde{\mathcal{G}}$ is derived from the diagram \mathcal{G} by removing all the external lines and disregarding the distinction of the type of lines. Suppose that a fundamental set of circuits (independent self-nonintersecting loops) of the chain diagram is known. Then, for i and j that label the lines of $\tilde{\mathcal{G}}$, B_{ij} is given by

$$U_{st} = \sum_k z_k \xi_{k,s} \xi_{k,t}, \quad U = \det_{st} U_{st}, \quad (\text{A.1})$$

$$B_{ij} = U \sum_{s,t} \xi_{i,s} \xi_{j,t} (U^{-1})_{st}. \quad (\text{A.2})$$

where s and t refer to the circuits. The loop matrix $\xi_{k,c}$ takes $(1, -1, 0)$ according to whether the line i is (along, against, outside of) circuit c . All lines are assumed to be appropriately directed.

The circuits are found in the following way. A maximal tree \mathcal{T} of a graph \mathcal{G} is a simply-connected set of lines that connects all vertices of \mathcal{G} and does not have loops. An example is shown in Fig. 5 where solid lines denote the maximal tree \mathcal{T} . For any pair of vertices there is a unique path on \mathcal{T} that links these vertices, because \mathcal{T} is simply-connected and if there

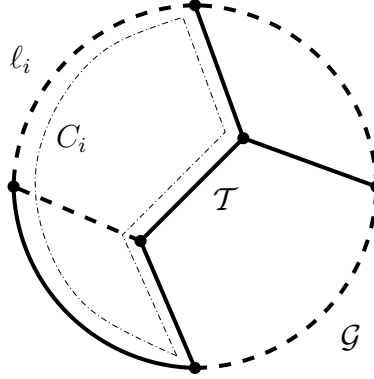


FIG. 5: A choice of maximal tree \mathcal{T} on graph \mathcal{G} is shown in solid lines. The chord set \mathcal{T}^* consists of the dashed lines. A circuit C_i is found for a line $\ell_i \in \mathcal{T}^*$ and a path on \mathcal{T} shown in thick lines that connects both ends of ℓ_i .

were more than one path \mathcal{T} would have a loop. \mathcal{T} consists of $n_v - 1$ lines where n_v is the number of vertices of \mathcal{G} .

The chord set (or cotree) \mathcal{T}^* is the complement of \mathcal{T} against \mathcal{G} , i.e., $\mathcal{T}^* \cap \mathcal{T} = \emptyset$ and $\mathcal{T}^* \cup \mathcal{T} = \mathcal{G}$. In Fig. 5 the lines in \mathcal{T}^* are shown by dashed lines. The number of lines of \mathcal{T}^* is $n_p - n_v + 1 = n_l$ where n_p and n_l are the number of lines and loops of \mathcal{G} , respectively. Then, for each $\ell_i \in \mathcal{T}^*$, there is a path \mathcal{P}_i on the tree \mathcal{T} which links two end-points of ℓ_i as shown above. ℓ_i and \mathcal{P}_i form a closed loop C_i . These closed loops are independent with each other by construction, namely, $\ell_i \notin C_j$ if $i \neq j$. They form a fundamental set of circuits.

For the diagrams without closed lepton loops (*q-type* diagrams) as described in Ref. [18], the fundamental set of circuits are found rather trivially. In this case the maximal tree \mathcal{T} is chosen as the set of lines that forms the open lepton line, and thus the chord set \mathcal{T}^* consists of the photon lines. Therefore, each circuit is identified by a photon line and a string of lepton lines that connects both ends of the photon line.

For a general diagram, a maximal tree of the diagram can be found in the following way. Choose a vertex v_0 of \mathcal{G} , and starting from v_0 , extend the tree by adding a line adjacent to the vertex of the tree, of which the other vertex is not yet included, until all vertices of \mathcal{G} are visited. During this process a unique path $\mathcal{P}(v_0, v_a)$, i.e. a string of lines in \mathcal{T} that runs from v_0 to v_a , is also found for each vertex v_a . A path on \mathcal{T} connecting an arbitrary pair of vertices v_a and v_b is then found by joining the paths $\mathcal{P}(v_b, v_0)$ and $\mathcal{P}(v_0, v_a)$ where $\mathcal{P}(v_b, v_0) \equiv \mathcal{P}^{-1}(v_0, v_b)$ is the string of lines of $\mathcal{P}(v_0, v_b)$ in reversed order. Note that the

duplicated lines in the paths are to be eliminated.

- [1] D. Hanneke, S. Fogwell, and G. Gabrielse, Phys. Rev. Lett. **100**, 120801 (2008).
- [2] T. Kinoshita and M. Nio, Phys. Rev. D **73**, 013003 (2006).
- [3] T. Aoyama, M. Hayakawa, T. Kinoshita, and M. Nio, Phys. Rev. Lett. **99**, 110406 (2007).
- [4] T. Aoyama, M. Hayakawa, T. Kinoshita, and M. Nio, Phys. Rev. **D77**, 053012 (2008).
- [5] K. Hagiwara, A. D. Martin, D. Nomura, and T. Teubner, Phys. Lett. **B649**, 173 (2007).
- [6] F. Jegerlehner and A. Nyffeler, Phys. Rept. **477**, 1 (2009).
- [7] M. Davier, A. Hoecker, B. Malaescu, C. Z. Yuan, and Z. Zhang, Eur. Phys. J. **C66**, 1 (2010).
- [8] B. Krause, Phys. Lett. **B390**, 392 (1997).
- [9] K. Melnikov and A. Vainshtein, Phys. Rev. **D70**, 113006 (2004).
- [10] J. Bijnens and J. Prades, Mod. Phys. Lett. **A22**, 767 (2007).
- [11] J. Prades, E. de Rafael, and A. Vainshtein, arXiv:0901.0306 [hep-ph].
- [12] A. Nyffeler, Phys. Rev. **D79**, 073012 (2009).
- [13] A. Czarnecki, B. Krause, and W. J. Marciano, Phys. Rev. Lett. **76**, 3267 (1996).
- [14] M. Knecht, S. Peris, M. Perrottet, and E. De Rafael, JHEP **11**, 003 (2002).
- [15] A. Czarnecki, W. J. Marciano, and A. Vainshtein, Phys. Rev. **D67**, 073006 (2003), **73**, 119901(E) (2006).
- [16] P. J. Mohr, B. N. Taylor, and D. B. Newell, Rev. Mod. Phys. **80**, 633 (2008).
- [17] T. Kinoshita and M. Nio, Phys. Rev. D **73**, 053007 (2006).
- [18] T. Aoyama, M. Hayakawa, T. Kinoshita, and M. Nio, Nucl. Phys. B **740**, 138 (2006).
- [19] T. Aoyama, M. Hayakawa, T. Kinoshita, and M. Nio, Nucl. Phys. **B796**, 184 (2008).
- [20] T. Aoyama, M. Hayakawa, T. Kinoshita, M. Nio, and N. Watanabe, Phys. Rev. **D78**, 053005 (2008).
- [21] T. Aoyama, M. Hayakawa, T. Kinoshita, and M. Nio, Phys. Rev. **D78**, 113006 (2008).
- [22] T. Aoyama, K. Asano, M. Hayakawa, T. Kinoshita, M. Nio, and N. Watanabe, Phys. Rev. **D81**, 053009 (2010).
- [23] P. Cvitanović and T. Kinoshita, Phys. Rev. D **10**, 3978 (1974).
- [24] P. Cvitanović and T. Kinoshita, Phys. Rev. D **10**, 3991 (1974).
- [25] T. Kinoshita, in *Quantum electrodynamics*, edited by T. Kinoshita (World Scientific, Singa-

- pore, 1990), pp. 218–321, (Advanced series on directions in high energy physics, 7).
- [26] T. Kinoshita and W. B. Lindquist, Phys. Rev. **D39**, 2407 (1989).
 - [27] J. A. M. Vermaseren, math-ph/0010025.
 - [28] G. P. Lepage, J. Comput. Phys. **27**, 192 (1978).
 - [29] S. Laporta and E. Remiddi, Phys. Lett. **B265**, 182 (1991).
 - [30] S. Laporta and E. Remiddi, Phys. Lett. **B301**, 440 (1993).
 - [31] M. Passera, Phys. Rev. D **75**, 013002 (2007).
 - [32] T. Kinoshita and M. Nio, Phys. Rev. **D70**, 113001 (2004).
 - [33] N. Nakanishi, *Graph theory and Feynman integrals* (Gordon and Breach, Science Publishers, New York, 1971).